

Coupled 1-D physical–biological model study of phytoplankton production at two contrasting time-series stations in the western North Pacific

Yoshikazu Sasai¹ · Chisato Yoshikawa² · S. Lan Smith^{1,3} · Taketo Hashioka¹ · Kazuhiko Matsumoto⁴ · Masahide Wakita⁵ · Kosei Sasaoka⁶ · Makio C. Honda⁴

Received: 2 June 2015 / Revised: 6 December 2015 / Accepted: 7 December 2015 / Published online: 9 January 2016
© The Oceanographic Society of Japan and Springer Japan 2016

Abstract A vertical one-dimensional physical–biological model is applied to clarify the mechanisms controlling the seasonality and interannual variability of primary production in the surface layer at two contrasting time-series stations, K2 (in the subarctic gyre) and S1 (in the subtropical gyre), in the western North Pacific. Using forcing based on realistic atmospheric and oceanic data, the model reproduces seasonal differences in the degree to which different controlling factors affect primary production between these two stations, primarily as a result of differences in the physical environment. At station K2, light intensity is an important factor controlling primary production in summer. After April, the mixed layer depth (MLD) becomes shallow, resulting in higher average light intensity, and the water column remains stratified until September; these sustain high primary production during this period. In contrast, at station S1, the supply of nutrients via entrainment is vital

to sustaining production, because light intensity remains sufficient throughout the year. In summer, the relationship between nutricline depth and euphotic layer is a controlling factor. The simulations forced by the different atmospheric conditions for each year, respectively, show different MLD. In the 2012 simulation, the deep winter MLD (200 m) enhances primary production in the surface layer as compared to the other two years (2010 and 2011) simulations.

Keywords Primary production · Seasonality · Interannual variability · A vertical one-dimensional physical–biological model · Western North Pacific

1 Introduction

Satellite imagery captures the large seasonal difference in surface phytoplankton production between the subarctic and subtropical gyre regions in the western North Pacific (e.g., Sasaoka 2002; Goes 2004). In this region, the strong western boundary currents, Kuroshio (subtropical gyre) and Oyashio (subarctic gyre), dominate. In the subarctic gyre, the peak of phytoplankton bloom occurs in the late spring or early summer. In the subtropical gyre, the phytoplankton bloom starts at the end of winter and the peak occurs at the beginning of spring (Siswanto 2014).

Differences in production between the two gyres result from differences in the physical environment (light intensity, ocean currents, and mixing), biogeochemical cycle (atmospheric CO₂ uptake, nutrients cycle, and biological pump), and physiology. In the subarctic gyre, the predominance of diatoms is a main reason why the biological pump and atmospheric CO₂ uptake are greater compared with the subtropical gyre (e.g., Honda 2002; Buesseler 2007; Honda and Watanabe 2010). From the 1990s, two

✉ Yoshikazu Sasai
ysasai@jamstec.go.jp

¹ Research and Development Center for Global Change, Japan Agency for Marine–Earth Science and Technology, 3173-25, Showa-machi, Kanazawa-ku, Yokohama 236-0001, Japan
² Department of Biogeochemistry, Japan Agency for Marine–Earth Science and Technology, Yokosuka, Japan
³ CREST, Japan Science and Technology Agency, Tokyo, Japan
⁴ Department of Environmental Geochemical Cycle Research, Japan Agency for Marine–Earth Science and Technology, Yokosuka, Japan
⁵ Mutsu Institute for Oceanography, Japan Agency for Marine–Earth Science and Technology, Mutsu, Japan
⁶ Research and Development Center for Global Change, Japan Agency for Marine–Earth Science and Technology, Yokosuka, Japan

subarctic time-series stations, station KNOT (44°N, 155°E) at the southwestern edge of subarctic gyre and station K2 (47°N, 160°E) (hereafter, Stn. K2) at the center of subarctic gyre after the end of observation at KNOT, have been operated in order to quantify CO₂ drawdown by the physical and biological pumps, and to understand the mechanisms underlying the biogeochemical cycle (Honda 2006; Bueseler 2007; Kawakami and Honda 2007). In the subtropical gyre, although shipboard observations have been carried out by Japan Meteorological Agency research vessels, multivariate biogeochemical observations typical of time-series stations were limited before the recent observation campaign from 2010 to 2013, the K2S1 project (Honda et al. 2015, this volume, a) (Fig. 1). The subtropical time-series station S1 (30°N, 145°E) (hereafter, Stn. S1) has been conducted from 2010 as part of this project. This comparative study has been conducted to examine the response of biogeochemical cycles and the lower-trophic ecosystem to different oceanic environments and climate change in the subarctic and subtropical gyre systems.

Before this project, no such comprehensive time-series study including simultaneous measurements of carbonate chemistry, phyto/zooplankton, primary productivity, and physical parameters in the western North Pacific had yet been performed in the subtropical gyre region of Stn. S1. Shipboard observation and sediment trap deployments (e.g., Honda 2015, this volume, b; Kawakami 2014; Wakita et al. 2015, this volume) as part of this project have captured seasonal differences and the different response of

biogeochemical tracers to external forcing. Some results of this project have been reported concerning the characteristics of biogeochemical cycles in the subarctic and subtropical gyres.

At Stn. K2 in the subarctic gyre, Matsumoto (2014) reported that the mean depth-integrated primary production is highest in summer and lowest in winter. The deep mixed layer in winter inhibits primary production by limiting light availability, whereas the primary production in summer increases under the greater average light intensity in the shallow mixed layer. Fujii (2014) investigated the role of iron availability for the phytoplankton community using a chemotaxonomy algorithm, microscopy, and fast-repetition-rate fluorometry around Stn. K2. The subarctic gyre in the North Pacific is well known as a high nutrient, low chlorophyll (HNLC) region (e.g., Martin 1994; Tsuda 2003; Harrison 2004), in which iron is known to limit biological production. They pointed out that the seasonal variability of phytoplankton community is mainly controlled by iron, with light and temperature limitation occurring in the winter and early spring.

At Stn. S1 in the subtropical gyre, the mean depth-integrated primary production is highest in winter, and is low in summer (Matsumoto et al. 2015, this volume). Strong winter mixing supplies nutrients from the subsurface layer to the euphotic layer, and therefore primary production increases. After the spring bloom depletes nutrients, the supply from the subsurface layer is weak, which leads to the formation of the subsurface chlorophyll maximum

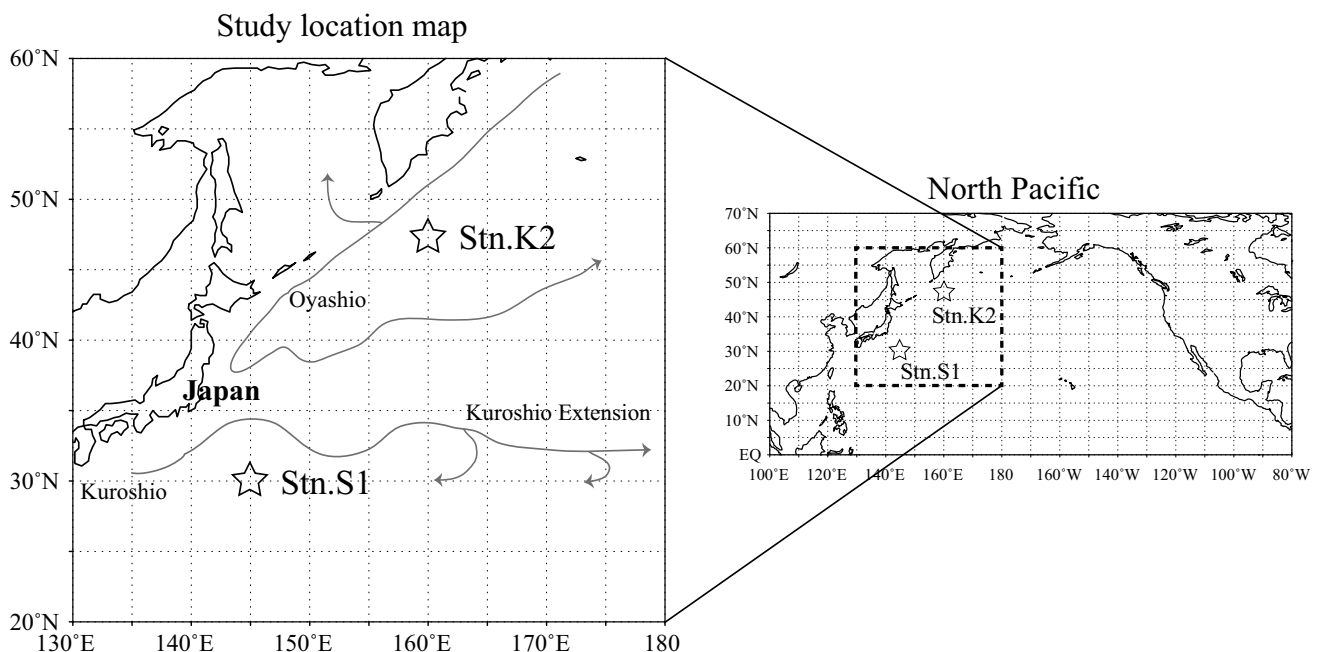


Fig. 1 Study location and map of two oceanic time-series stations (Stn. K2: 47°N, 160°E and Stn. S1: 30°N, 145°E) in the western North Pacific

near the nutricline depth in summer. Matsumoto et al. also reported that annually averaged primary production in the surface layer was of the same level at Stns. K2 and S1, despite the large difference in the seasonal variation of primary production. Kawakami (2014) investigated the sinking fluxes of particulate organic carbon (POC) estimated from ^{210}Po and ^{210}Pb radioactivity. The result implied that the efficiency of the biological pump is larger at Stn. K2 than at Stn. S1. The estimation of particle sinking flux using the sediment traps showed the same results (Honda 2015, this volume b).

The comparative time-series observations at Stns. K2 and S1 revealed two characteristics: (1) annual primary production in the surface layer at Stn. K2 was of the same level as at Stn. S1, despite different physical and biogeochemical environments. However, (2) the biological pump at Stn. K2 was more efficient than at Stn. S1. In this study, we applied a simple one-dimensional (1-D) coupled physical–biological model to clarify the two mechanisms above. Modeling is an effective approach to study biogeochemical cycles, by testing the effects of different physical and biological processes at time-series stations. Several previous studies have applied ecosystem models to time-series stations in the North Pacific to examine ecosystem dynamics (e.g., Kawakami 1997; Fujii 2002; Kishi et al. 2007; Shigemitsu 2012). In addition, several recent biogeochemical modeling studies have been conducted incorporating the iron cycle into their marine ecosystem models, to clarify the relationships among carbon, nutrients, and iron fluxes and to investigate the role of iron in limiting biological productivity (e.g., Moore 2004; Parekh et al. 2002; Shigemitsu 2012). However, observational data of iron needed to constrain biogeochemical models are limited, because it is difficult to accurately measure dissolved iron concentrations, and because of the large uncertainties that remain about key processes within the iron cycle (e.g., Boyd and Ellwood 2010) and about how iron affects different phytoplankton groups (Boyd 2010). Our model does not include the iron cycle explicitly, given that iron concentrations have not been observed at these time-series stations. Alternatively, by optimizing parameters associated with biological productivity for Stns. K2 and S1, based on data from in situ observations, the model implicitly accounts for the limitation of biological productivity by iron at Stn. K2.

Our study objective is to investigate the mechanisms controlling the seasonality and interannual variability of primary production in the surface layer at Stn. K2 (subarctic gyre) and Stn. S1 (subtropical gyre) in the western North Pacific. We concentrate on the role of light availability and nutrient supply for surface primary production as controlled by the development of the mixed layer, through comparison of observation data obtained in this project. We focus on the 1-D physical process of vertical winter mixing

as it impacts primary production, without explicitly considering 3-D physical processes.

2 Methods

A 1-D mixed layer model is applied to simulate the seasonal variability of the upper ocean at two time-series stations (Stns. K2 and S1) in the western North Pacific. The mixed layer model is a Mellor–Yamada level 2.5 (Mellor and Yamada 1982), which resolves 105 vertical levels, each of 5 m thickness, near the surface and increasing to 250 m at the bottom (5500 m) of the model domain. Initial conditions for temperature and salinity in the mixed layer model are taken from the World Ocean Atlas 2009 (WOA09) (Antonov 2010, Locarnini 2010). The model is forced by wind stress, heat flux, and fresh water flux from a Japanese 25-year reanalysis (JRA25) (Onogi 2007) from 2010 to 2012 (Fig. 2) and the model time step is 15 min.

A nitrogen-based pelagic plankton ecosystem model (Kawakami 1997; Yoshikawa et al. 2005) was modified by adding diatoms and the associated silicate cycle (Fig. 3), resulting in nine compartments (nitrate, NO_3 ; ammonium, NH_4 ; silicic acid, Si; two categorized phytoplankton: small phytoplankton, PS and large phytoplankton, PL; one zooplankton, Z; particulate organic nitrogen, PON; dissolved organic nitrogen, DON; and bio-silicate, BSi). In the North Pacific, silicate is an important limiting nutrient for diatoms (PL). The model represents cycles of nitrogen and silicon simultaneously. Phytoplankton growth rate is formulated as a function of light intensity (from JRA25, above), temperature, and NO_3 , NH_4 , and Si concentrations. The other biological processes are formulated as functions of temperature as well as nitrogen and silicon concentrations. The PON and BSi consist of mortality of phytoplankton and zooplankton and egestion of zooplankton (see "Appendix" for details).

Initial estimates for biological parameters were from Kishi et al. (2007). Parameter values (Table 1) were then tuned to reproduce the seasonal variability of nutrients (NO_3 , NH_4 , and Si), chlorophyll, and primary production in the upper ocean simultaneously based on the K2S1 project in situ observation data. The evolution of each biological tracer concentration governed by a vertical mixing is calculated by a vertically 1-D mixed layer model (no vertical advection), with source-minus-sink terms as described in the "Appendix". The initial NO_3 and Si are taken from the climatological data of WOA09 (Garcia 2010). The initial NH_4 is set to $1.0 \text{ mmol N m}^{-3}$ in this study. The initial values of PS, PL, and Z are set to $0.2 \text{ mmol N m}^{-3}$ at the surface, decreasing exponentially with a scale depth of 100 m (Sarmiento 1993). PON, DON, and BSi are initialized to $0.1 \text{ mmol N m}^{-3}$ at every depth (0–5500 m). The

Fig. 2 Time series of **a** surface short wave radiation ($W m^{-2}$) and **b** wind speed ($m s^{-1}$) at two oceanic time-series station (black line for Stn. K2 and red line for Stn. S1) from JRA25

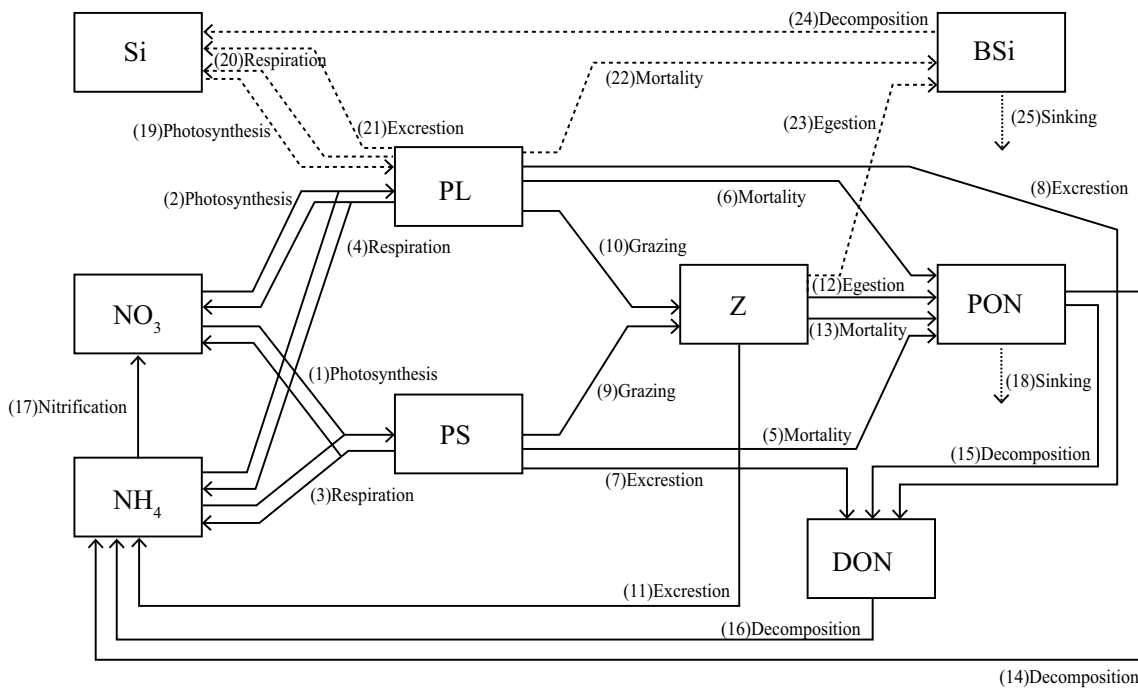
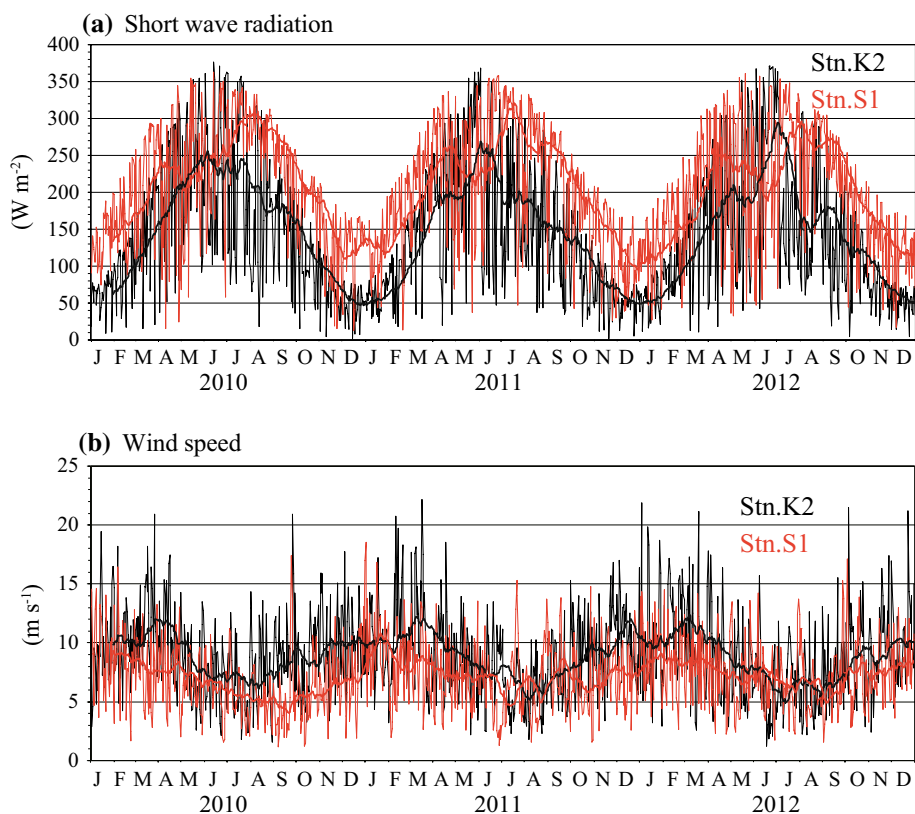


Fig. 3 Schematic diagram of ecosystem model. Solid black arrows indicate nitrogen flow (1–17) and dashed black arrows indicate silicate flows (19–24). Dotted black arrows are sinking particles (18 and 25). Biological model equations are described in the "Appendix"

coupled 1-D physical–biological model was integrated for a 5-year spin-up period using data from 2010 from the JRA25 data set. The values during last year of that coupled

5-year integration were then used as the initial conditions for all biological tracers, and the coupled model was forced by JRA25 from 2010 to 2012. Three years (2010–2012)

Table 1 Parameters of ecosystem model

	Symbol	Value	Unit
<i>Parameters for PS and PL</i>			
Ratio of nitrate to chlorophyll	Rnchl _a	1.59	No dim
Optimum light intensity for PS and PL	I_{opt}	100	W m ⁻²
PS potential maximum uptake rate (#)	V _{maxS}	0.52 (K2), 1.0 (S1)	day ⁻¹
PL potential maximum uptake rate (#)	V _{maxL}	0.72 (K2), 1.5 (S1)	day ⁻¹
Initial slope of NO ₃ for PS (#)	A_{NO3PS}	2.0 (K2), 2.0 (S1)	No dim
Initial slope of NH ₄ for PS (#)	A_{NH4PS}	20.0 (K2), 20.0 (S1)	No dim
Initial slope of NO ₃ for PL (#)	A_{NO3PL}	1.0 (K2), 1.0 (S1)	No dim
Initial slope of NH ₄ for PL (#)	A_{NH4PL}	10.0 (K2), 10.0 (S1)	No dim
Initial slope of Si for PL (#)	A_{SiPL}	1.0 (K2), 1.0 (S1)	No dim
Temperature coefficient for photosynthetic rate for PS and PL	κ_{GppS} , κ_{GppL}	0.0693	°C ⁻¹
Ammonium inhabitation coefficient for PS and PL	φ_{PS} , φ_{PL}	1.5	($\mu\text{mol N l}^{-1}$) ⁻¹
Respiration rate at 0 °C for PS and PL	r_{PS} , r_{PL}	0.03	day ⁻¹
Temperature coefficient for respiration rate for PS and PL	κ_{ResS} , κ_{ResL}	0.0519	°C ⁻¹
Mortality rate at 0°C for PS	μ_{PS}	0.0585	($\mu\text{mol N l}^{-1}$) ⁻¹ day ⁻¹
Mortality rate at 0°C for PL	μ_{PL}	0.029	($\mu\text{mol N l}^{-1}$) ⁻¹ day ⁻¹
Temperature coefficient for mortality rate for PS and PL	κ_{MorS} , κ_{MorL}	0.0693	°C ⁻¹
Extracellular excretion rate of PS and PL	γ_{PS} , γ_{PL}	0.135	No dim
<i>Parameters for Z</i>			
Maximum grazing rate on PS and PL at 0 °C	GR _{max}	0.3	day ⁻¹
Temperature coefficient for grazing rate for PS and PL	κ_{GraPS} , κ_{GraPL}	0.0693	°C ⁻¹
PS and PL zooplankton Ivlev constant	λ_{PS} , λ_{PL}	1.4	($\mu\text{mol N l}^{-1}$) ⁻¹
Zooplankton threshold value for grazing on PS and PL	P2Z	0.04	($\mu\text{mol N l}^{-1}$) ⁻¹
Assimilation efficiency of Z	α	0.7	No dim
Growth efficiency of Z	β	0.3	No dim
Mortality rate at 0 °C for Z	μ_Z	0.0585	($\mu\text{mol N l}^{-1}$) ⁻¹ day ⁻¹
Temperature coefficient for mortality rate for Z	κ_{MorZ}	0.0693	°C ⁻¹
<i>Parameters for PON, DON, BSi etc.</i>			
Nitrification rate at 0 °C (#)	Nit ₀	0.15	day ⁻¹
Temperature coefficient for nitrification	κ_{Nit}	0.0693	°C ⁻¹
Decomposition rate at 0 °C from PON to NH ₄	VP2N ₀	0.1	day ⁻¹
Temperature coefficient for decomposition from PON to NH ₄	κ_{P2N}	0.0693	°C ⁻¹
Decomposition rate at 0 °C from PON to DON	VP2D ₀	0.1	day ⁻¹
Temperature coefficient for decomposition from PON to DON	κ_{P2D}	0.0693	°C ⁻¹
Decomposition rate at 0 °C from DON to NH ₄	VD2N ₀	0.2	day ⁻¹
Temperature coefficient for decomposition from DON to NH ₄	κ_{D2N}	0.0693	°C ⁻¹
Decomposition rate at 0 °C from BSi to Si	VP2Si ₀	0.1	day ⁻¹
Temperature coefficient for decomposition from BSi to Si	κ_{P2Si}	0.0693	°C ⁻¹
POC(mg):Si(mg) ratio (#)	R _{POCSi}	0.05 (K2), 0.15 (S1)	No dim
Si:N ratio (#)	R _{sin}	1.5 (K2), 0.6 (S1)	No dim
N:C ratio (#)	R _{nc}	16/106	No dim
Sinking velocity of PON and BSi (#)	W _S	30 (to 1000 m)	m day ⁻¹

These parameters used for each biological process equation in “Appendix”

#, Parameter values are estimated from in situ observation data and other parameter values are taken from Kishi et al. (2007)

were averaged to obtain one seasonal cycle, which was compared with in situ observation data (e.g., Honda 2015, this volume b; Matsumoto 2014, this volume; Wakita et al. this volume).

Although iron availability is known to limit phytoplankton productivity near Stn. K2 (Fujii 2014), we have not explicitly incorporated equations to represent the iron cycle, because of the lack of quantitative observations of biologically available iron concentrations at these sites and the large uncertainty about its rate of supply (Takeda 2006; Smith 2009; Shigemitsu 2012). Our focus here is on the seasonal and interannual variations in biological production, for which the hypothesis can be largely represented by light and the upwelling of nutrients from deeper waters. Iron is upwelled together with nitrogen, silicic acid and other nutrients, which suggests that it may not be necessary to explicitly resolve the iron cycle in order to capture the overall trends in chlorophyll and primary production, as found in other studies (Takeda 2006; Smith et al. 2010). We have therefore implicitly represented iron limitation at Stn. K2 by applying a lower maximum growth rate compared to that applied for Stn. S1 (Table 1). Thus, for Stn. K2, we effectively assumed a constant degree of iron limitation throughout the seasonal cycle, just as in previous studies applied to other locations (Denman and Peña 1999; Denman 2006). This degree of

effective iron limitation is tunable by adjusting the maximum growth rate.

3 Results and discussion

3.1 Physical environment

The 3-year mean (2010–2012) of simulated physical and biological tracer distributions at Stn. K2 (subarctic region) and Stn. S1 (subtropical region) in the western North Pacific compared with data from in situ observations are shown in Figs. 4, 5 and 6. Simulated vertical distribution of temperature and mixed layer depth (MLD, which is defined as the depth at which the temperature becomes $0.2\text{ }^{\circ}\text{C}$ less than the SST) clearly reproduce the seasonality at Stns. K2 and S1 (Fig. 4). At Stn. K2, sea surface temperature decreases by approximately $3\text{ }^{\circ}\text{C}$ as the MLD deepens to a maximum of 150 m depth in winter, and summer temperature reaches $14\text{ }^{\circ}\text{C}$ with the surface heating. Summer MLD is 10 m. This is similar to the seasonal variability of observed temperature: $2\text{ }^{\circ}\text{C}$ in winter with a maximum MLD of 150 m, and $12\text{ }^{\circ}\text{C}$ in summer with a minimum MLD of 10 m. However, the observed temperature presented about $1\text{ }^{\circ}\text{C}$ around 100 m (Fig. 4a) through the year; the model does not reproduce the low temperature because the model cooling might

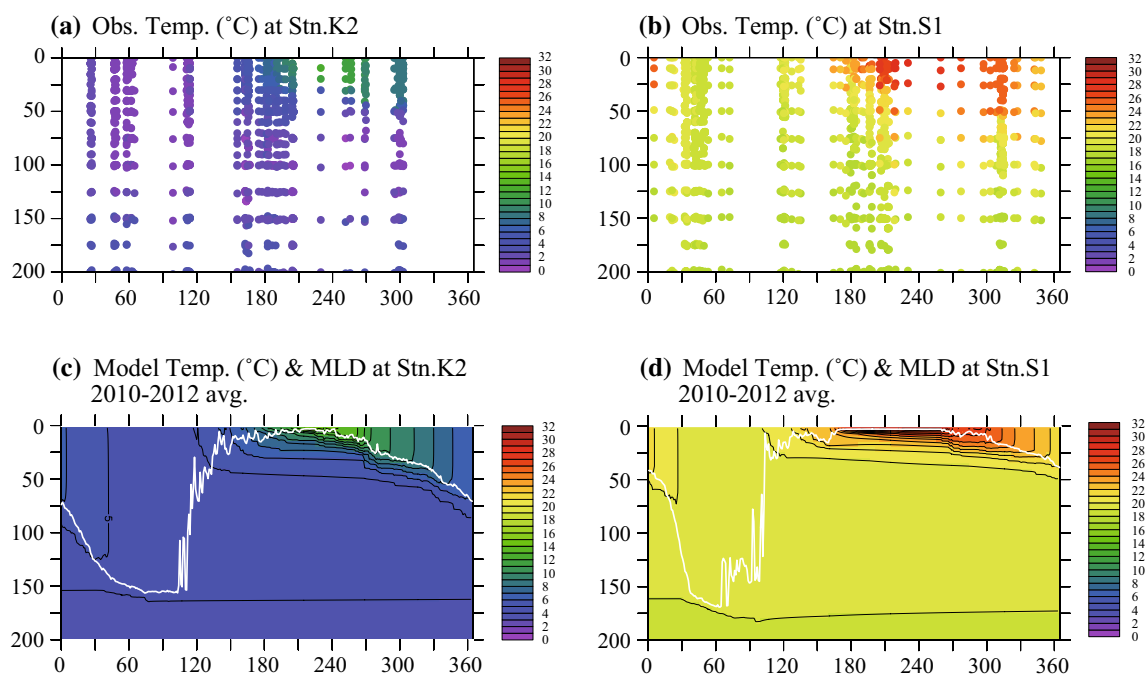


Fig. 4 Seasonal cycle of vertical temperature ($^{\circ}\text{C}$) from **a**, **b** in situ observation and **c**, **d** 1-D model at Stns.K2 and Stn. S1. *White line* in the model temperature indicates mixed layer depth (m). *Circles* are

observed values at each day of the year between 2005 and 2013 at Stn. K2, and between 2010 and 2013 at Stn. S1 and depth

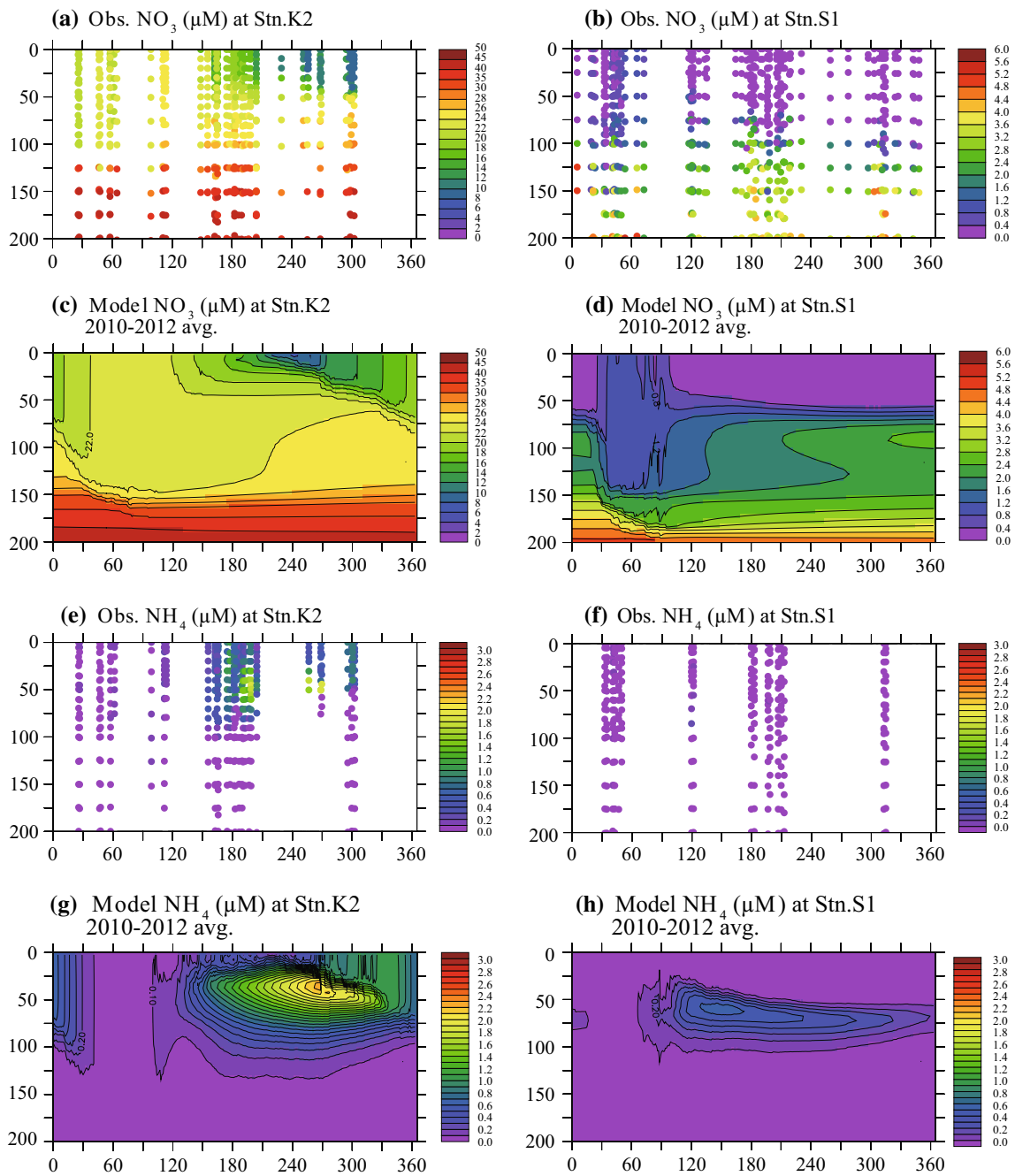


Fig. 5 Seasonal cycle of nitrate concentration (μM) and ammonium (μM) from **a, b, e, f** in situ observation and **c, d, g, h** 1-D model at Stns. K2 and S1. Color interval of nitrate concentration is from 0 to

$50 \mu\text{M}$ at Stn. K2 and from 0 to $6 \mu\text{M}$ at Stn. S1. Circles are observed values at each day of the year between 2005 and 2013 at Stn. K2, and between 2010 and 2013 at Stn. S1 and depth.

be weak. At Stn. S1, both the modelled winter MLD (175 m depth) and the observed value of 200 m in February (Wakita et al. this volume) are deeper than at Stn. K2. Seasonal variability of modelled temperature at Stn. S1 varies from 20°C in winter to 28°C in summer in the surface layer. The observed temperature shows that warm water (24°C) extends to 75 m depth, but the stretch of simulated warm water is somewhat more shallow because the 1-D mixed

layer model does not include 3-D advection and diffusion processes, only extending down to 50 m depth (Fig. 4b, d).

3.2 Seasonal nutrient dynamics

Simulated vertical distribution of nutrients (NO_3 , NH_4 , and Si) and chlorophyll presents similar seasonal variability as seen in the observations at Stns. K2 and S1 (Figs. 5,

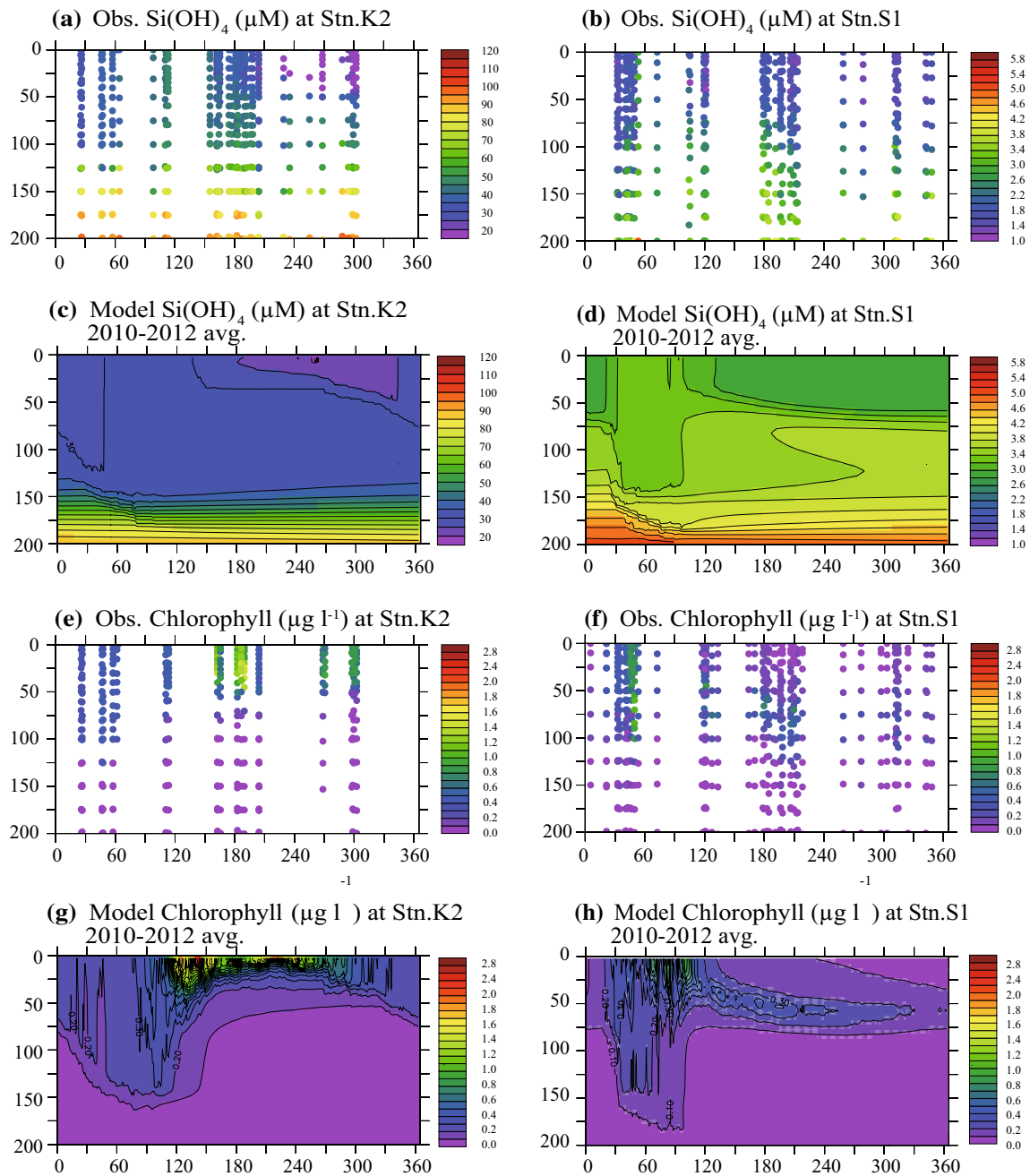


Fig. 6 Seasonal cycle of silicate concentration (μM) and chlorophyll (μl^{-1}) from **a, b, e, f** observation and **c, d, g, h** 1-D model at Stns.K2 and S1. Color interval of silicate concentration is from 10 to 120 μ

M at Stn. K2, and from 1 to 6 μM at Stn. S1. Circles are observed values at each day of the year between 2005 and 2013 at Stn. K2, and between 2010 and 2013 at Stn. S1 and depth

6, Wakita et al. this volume). At both stations, in winter, nutrient concentrations increase with the development of MLD before the spring bloom. From spring through summer, nutrients are depleted in the surface layer as phytoplankton takes up nutrients for growth. The subsurface maximum of NH_4 in summer and autumn is formed by the balance of nitrification, photosynthesis minus respiration (decrease of NH_4), and decomposition (increase of

NH_4). In the subsurface maximum depth, the decomposition flux in the subsurface layer is larger than nitrification and photosynthesis minus respiration fluxes. At Stn. K2, modelled NO_3 in the surface layer therefore decreases from 24 μM in winter to 10 μM in summer, and modelled NH_4 , which is maximal in the subsurface, increases from 0.1 μM in winter to 2.4 μM in summer, which is slightly higher than the observed subsurface maximum of NH_4 (1.8 μM).

The surface observed NO_3 in summer decreases to 6–8 μM , but the minimum of modelled NO_3 is 10 μM . Modelled Si also decreases from 32 μM in winter to 20 μM in summer, but the minimum of modelled Si is slightly larger than observed. In the surface layer (within the shallow MLD), modelled high chlorophyll ($>1.4 \mu\text{g l}^{-1}$) appears from May to August. The bloom season is well reproduced in the model. Although there is no observation of chlorophyll in May, the decrease of NO_3 and Si corresponds to the increase of chlorophyll in May (Figs. 5a, c, 6a, c, e, g). At Stn. S1, high NO_3 and Si in the surface layer are controlled by the winter MLD, and decreased by the biological production in spring. Modelled NO_3 in winter rapidly increases from 0.1 to 1.2 μM . At the same time, simulated Si also increases from 2.4 to 4.0 μM with the development of MLD. The seasonal variability of modelled NO_3 and Si in the surface layer is similar to observed NO_3 and Si. But, the decrease of Si after spring is not reproduced. The modelled Si cycle is only connected with PL and BSi. In the model, phytoplankton may not take up enough Si to sufficiently deplete its concentration, although this is not clear based on the sparse observation of Si. Maximal NH_4 in the subsurface layer occurs from May to November, but the modelled values are larger than observed. Modelled chlorophyll shows the high concentration ($>1.0 \mu\text{g l}^{-1}$) in late winter and spring and a subsurface maximum (0.3 $\mu\text{g l}^{-1}$) layer around 50 m in late spring and summer. The pattern of seasonal variability is strongly reflected by the variability of vertical nutrient distributions. Observed subsurface maximum chlorophyll layer forms around 75 m, and the maximum concentration is close to 1.0 $\mu\text{g l}^{-1}$ (Fig. 6f). However, the modelled maximum chlorophyll layer is around 50 m (Fig. 6h), because the modelled 1.2 μM of NO_3 line (50 m, hereafter, this line is nutricline in the model) is shallower than observed (75 m) (Fig. 5d).

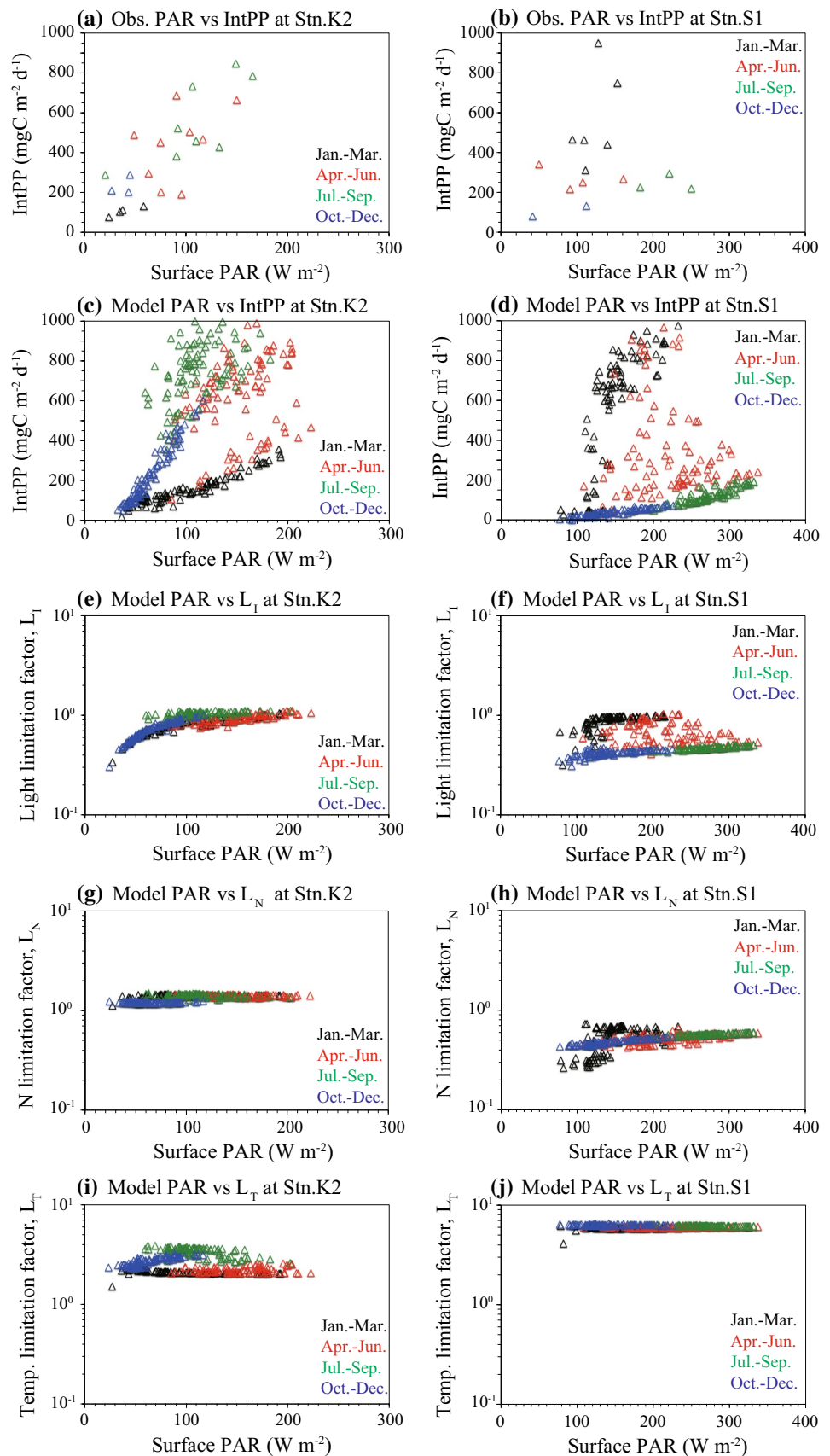
The seasonal change of MLD directly works the variability of vertical nutrient distributions (Figs. 5, 6) at both stations. In areas deeper than MLD, the modelled vertical distribution of nutrients does not change because this 1-D mixed layer model does not include 3-D physical processes (advection and diffusion) and because the vertical mixing is weak below the MLD (Figs. 5c, d, 6c, d). Because the vertical distribution of nutrients below MLD does not change, the modelled period of high chlorophyll is shorter than observed during summer at Stn. K2, and the modelled subsurface maximum chlorophyll layer at Stn. S1 is shallower than observed. The depletion of nutrients in summer and autumn in the surface layer is mainly controlled by biological production (or phytoplankton growth rate). Based on tuning of the model parameters to match model output to the observations and considering that phytoplankton are iron limited at Stn. K2 (Fujii 2014), we applied maximum growth rates for phytoplankton at Stn. K2, which were

approximately half their values applied at Stn. S1 (Table 1). This suppresses the uptake of the macronutrients nitrate and silicic acid by a constant factor throughout the year at Stn. K2 and allows the model to reproduce the low concentrations of those macronutrients during summer. Iron limitation can also increase the Si:N ratio of diatoms, and thus affect the drawdown of Si and patterns of nutrient limitation (Takeda 2006; Smith et al. 2010). Our model includes only one compartment of diatoms, PL, with a constant Si:N ratio, and biogenic silica, BSi. This is likely the reason why the model agrees better with the observed concentrations of nitrate, compared to those of silicate.

3.3 Factors controlling primary production

To investigate the factors that control primary production, hereafter considered as gross primary production minus respiration (the first and second terms of Eqs. 1, 2 in "Appendix"), we have focused on its relationships to the limitation factors for light intensity, L_I , nutrient concentration, L_N , and temperature, L_T , integrated over depth within the near-surface layer (Fig. 7). Matsumoto (2014) reported that light intensity is an important control factor for the seasonal variability of primary production and phytoplankton biomass in the western Pacific subarctic gyre. Similarly, we compare the surface light intensity (PAR) with depth-integrated primary production (Figs. 7a–d). At Stn. K2, depth-integrated (0–150 m) primary production increases with the surface light intensity (Figs. 7a, c), in both the observations and model. Previous results in the western Pacific subarctic region have likewise found a strong positive relation between primary production and light intensity (Matsumoto 2014). Our model results also reveal the seasonal variability of primary production. From January to April, primary production is light-limited because of the deep MLD, which keeps PAR low throughout the water column. The limitation factor, L_I , for phytoplankton growth rate in the model (Fig. 7e, Eqs. 10, 11 in "Appendix") has a similar effect (when PAR is low, light-limited growth rate is small), and its effect changes seasonally. Hence, the chlorophyll concentration remains low (Fig. 6g) throughout the water column (Fig. 4c) until April. After April, the MLD becomes shallow and stratification develops, which raises light intensity sufficiently for primary production to increase and remains high from May through November (Figs. 4c, 7c). L_I (Fig. 7e) is also high and L_T (Fig. 7i) increases from winter to summer. The initial slope of relation between primary production and light intensity becomes steep from winter (black triangle) to summer (green triangle) in Fig. 7c. The nitrate concentration within the MLD does not limit primary production at Stn. K2 (Figs. 5a, c, 6e, g, 7g), because nitrate remains sufficient and nitrate-limitation factor, L_N , of growth rate changes little. Therefore, the

Fig. 7 Relationship between depth-integrated (from 0–150 m at Stn. K2 and 0–200 m at Stn. S1) primary production ($\text{mg C m}^{-2} \text{ day}^{-1}$) and surface PAR (W m^{-2}) at Stns. K2 and S1: **a, b** in situ observations, and **c, d** the 1-D model. Breakdown of the depth-integrated limitation factors for of phytoplankton growth rate (and hence primary production) from the model plotted versus surface PAR at Stns. K2 and S1: **e, f** light limitation factor, L_I , **g, h** nutrient limitation factor, L_N , and **i, j** Temperature limitation factor, L_T . Modelled primary production is proportional to the product of these three limitation factors and the phytoplankton concentration (see growth rate Eqs. 10, 11 in “Appendix”). All limitation factors are plotted with a logarithmic (\log_{10}) scale on the vertical axis



seasonal variability of light intensity mainly controls primary production.

Conversely, at Stn. S1, depth-integrated (0–200 m) primary production is not strongly related to surface light intensity during winter and spring (Fig. 7b, d), because both the degree of nutrient limitation and the MLD vary during this time. However, during summer and autumn when production is low because of relatively constant nutrient limitation, and while the MLD remains relatively shallow, production is more strongly related to light intensity. Nitrate, which does not vary much over the seasonal cycle, is the primary limiting factor (Fig. 7h). When PAR is close to 120 (observed) or 150 (model) W m^{-2} in winter (black triangle), the integrated primary production in both observation and model is over $600 \text{ mg C m}^{-2} \text{ day}^{-1}$. Growth rate is already saturated with respect to light at around 150 W m^{-2} ; however, growth rate still increases with increasing nitrate (Fig. 7f, h). The comparison of the vertical nitrate and chlorophyll distributions also shows that nitrate concentration is an important limiting factor for primary production (Figs. 5, 6). During winter, nitrate, which is supplied by the deepening of the MLD correlates strongly with primary production. After April, chlorophyll in the subsurface maximum, which appears from May to November, also correlates strongly with the nutricline depth (Figs. 4d, 5d, 6h). Depth-integrated primary production and PAR are therefore positively correlated. In contrast to light and temperature, growth rate is not correlated with L_T (Fig. 7f, j). Changes in nitrate have a greater impact on growth rate than do changes in light levels, and therefore the nutricline depth is a key factor for primary production. Matsumoto et al. (this volume) found a significant negative correlation between the depth of nitrate depletion and depth-integrated primary production, and the depth of nitrate depletion deepened with time after winter. The degree of L_N therefore depended very much on the season. The potential photosynthetic activity, quantified in terms of F_v/F_m , was remarkably reduced in the surface stratified water during summer and autumn (Fujiki et al. this volume). This implies that nutrient limitation was enhanced due to the development of stratification. The seasonal variability of modelled nutrients and chlorophyll are consistent with the observation-based results at Stn. S1.

3.4 Variability of primary production

Interannual variability of primary production (in situ observation, satellite data, and model), MLD (in situ observation and model), modelled f -ratio [the ratio of NO_3 uptake to total N ($\text{NO}_3 + \text{NH}_4$) uptake] and modelled e -ratio (the ratio of export production to depth-integrated primary production) are shown in Fig. 8. The model captures the weak inter-annual variation of primary production as a function

of the inter-annual differences in physical forcing, in agreement with the observations. In situ MLD also shows weak inter-annual variation. During the 3-year simulations (2010–2012), the surface short wave radiation and wind speed at Stns. K2 and S1 show clear seasonality and inter-annual variability (Fig. 2), and the simulated MLD shows corresponding variability (Fig. 8i, j).

At Stn. K2, the in situ observations capture the peak of depth-integrated (0–150 m) primary production (about $800 \text{ mg C m}^{-2} \text{ day}^{-1}$) during summer (Fig. 8a), and its magnitude is similar for all 3 years. The peak productivity of the satellite-based estimates occurs in late summer (over $1200 \text{ mg m}^{-2} \text{ day}^{-1}$ in Fig. 8c), and its seasonal variability is similar for all 3 years. The model reproduces similar seasonal variability of observed primary production (Fig. 8a, e); however, the modelled primary production is overestimated throughout the annual cycle. The maximum primary production in the model is close to $1200 \text{ mg C m}^{-2} \text{ day}^{-1}$ (50 % greater than observed and close to satellite data) and the peaks appear in the late spring and autumn. The first peak of primary production occurs during late spring when nutrients are abundant, and in terms of nitrogen, it is mostly new production (f ratio = 0.7 in Fig. 8k). In the model, the second (during summer or autumn) peak of primary production is supported by N-recycling (f ratio = 0.4 in Fig. 8k). The efficiency of the biological pump is high in winter and autumn and is low in spring and summer (Fig. 8m). The efficiency in winter is related to new production and the efficiency in summer is linked to N-recycling (Fig. 8k, m). Although our implicit assumption of a constant degree of iron limitation at Stn. K2, as embodied in a lower maximum growth rate compared to Stn. S1, allows a reasonable reproduction of the spring bloom and overall annually averaged production, it also results in an over-estimate of production during the autumn. This is because iron is depleted starting with the spring bloom through summer, and iron limitation becomes more severe during the autumn (Fujii 2014). Therefore, in order to resolve the detailed seasonal pattern of production in the subarctic gyre, it may be necessary to explicitly model the concentration of bio-available iron and the iron cycle. Modelled primary production has only weak interannual variability. The model also reproduces a similar f -ratio and e -ratio for all three years, and the changes in nitrate concentration driven by differences in MLD have little effect.

The comparison of seasonally averaged depth-integrated primary production between in situ observations and the model is listed in Table 2 (Stn. K2). Averages for the model were calculated using the same dates as the corresponding observations, for each season (Fig. 8a, b, e, f). The observed primary production is maximal in summer and minimal in winter. Although the model reproduces the seasonal variation of primary production, it overestimates its value by

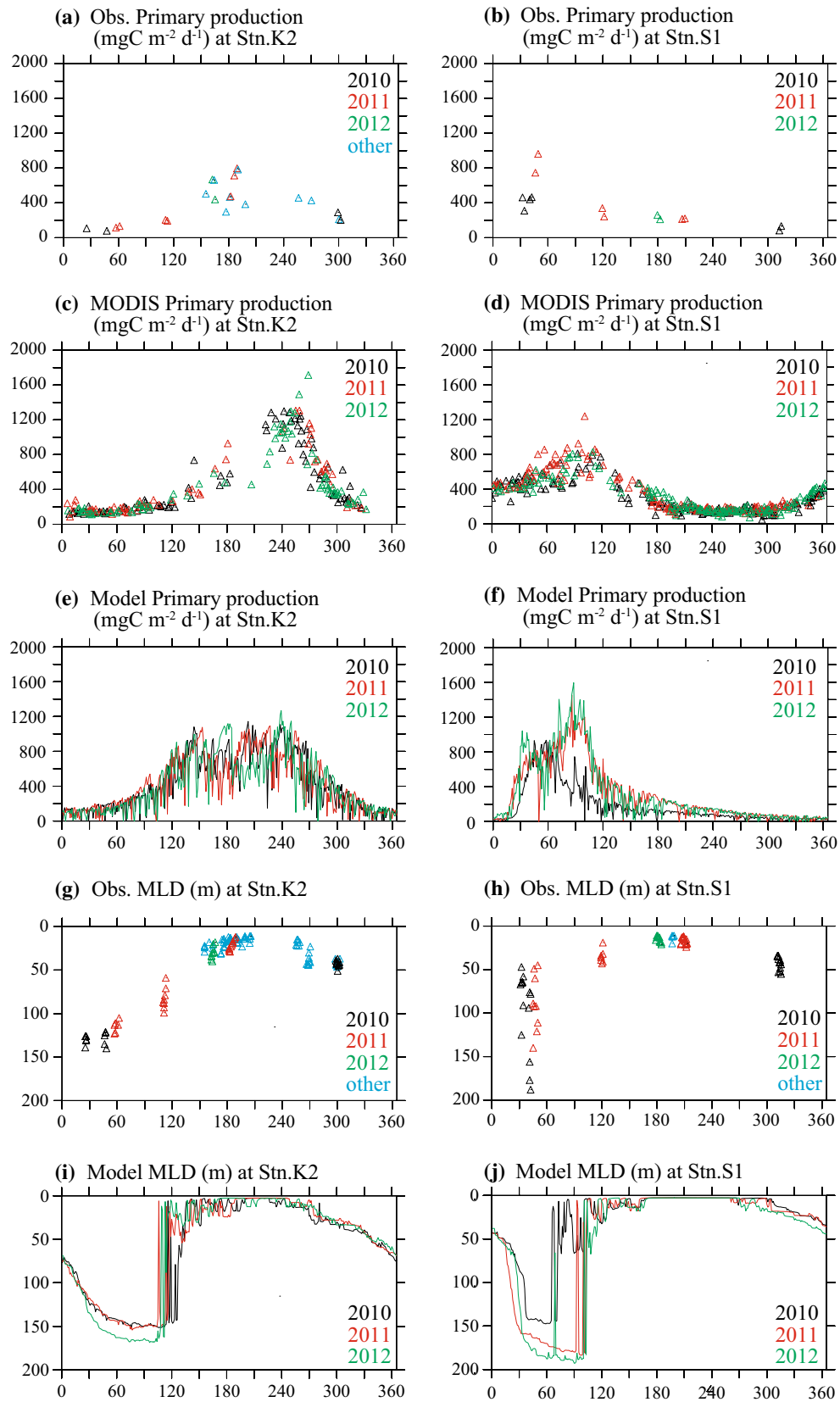


Fig. 8 Time series of depth-integrated primary production ($\text{mg C m}^{-2} \text{ day}^{-1}$) from **a, b** in situ observation, **c, d** satellite-based estimates and **e, f** 1-D model, **g, h** in situ observation MLD (m), **i, j** 1-D model MLD (m), **k, l** *f*-ratio of 1-D model, and **m, n** *e*-ratio of 1-D model at Stns.K2 and S1 for respective years 2010, 2011 and 2012. Vertical scale of *e*-ratio **m, n** is logarithmic (\log_{10}). Satellite primary production is computed with the vertically generalized production model (VGPM) of Behrenfeld and Falkowski (1997). Satellite data (chlorophyll-*a*, PAR, and sea surface temperature) in VGPM were obtained from NASA Ocean Color Web site (<http://oceancolor.gsfc.nasa.gov>) and the Remote Sensing Systems (<http://www.remss.com/measurements/sea-surface-temperature>)

about 20–70 % compared to in situ observation over the three years simulated. Especially, after summer (July), this is largely because the model predicts unrealistic summer and autumn blooms, which result from the assumption of a constant degree of iron limitation throughout the year at Stn. K2. In addition, nutrient (NH_3 and NH_4)

concentrations in this model are high because of fast N recycling (Figs. 5c, g, 8e, k).

At Stn. S1, the observations show large seasonal variability of primary production. However, the inter-annual variability of primary production and MLD are unclear because of the limited number of in situ observations (Figs. 8b, h). The satellite-based estimates show one peak in early spring ($1000 \text{ mg C m}^{-2} \text{ day}^{-1}$ in Fig. 8d) and relatively large magnitude of primary production during autumn compared with in situ observation and model. The model captures the large interannual variability of primary production (Fig. 8f), which results from year-to-year variations in the simulated MLD (Fig. 8j). Simulated primary production peaks in winter and early spring. The first peak is consistent with the observations, but the depth-integrated primary production in the model ($1200\text{--}1600 \text{ mg C m}^{-2} \text{ day}^{-1}$) is greater than observed ($1000 \text{ mg C m}^{-2} \text{ day}^{-1}$). In 2011 and 2012, the MLD is 50 m deeper than in 2010,

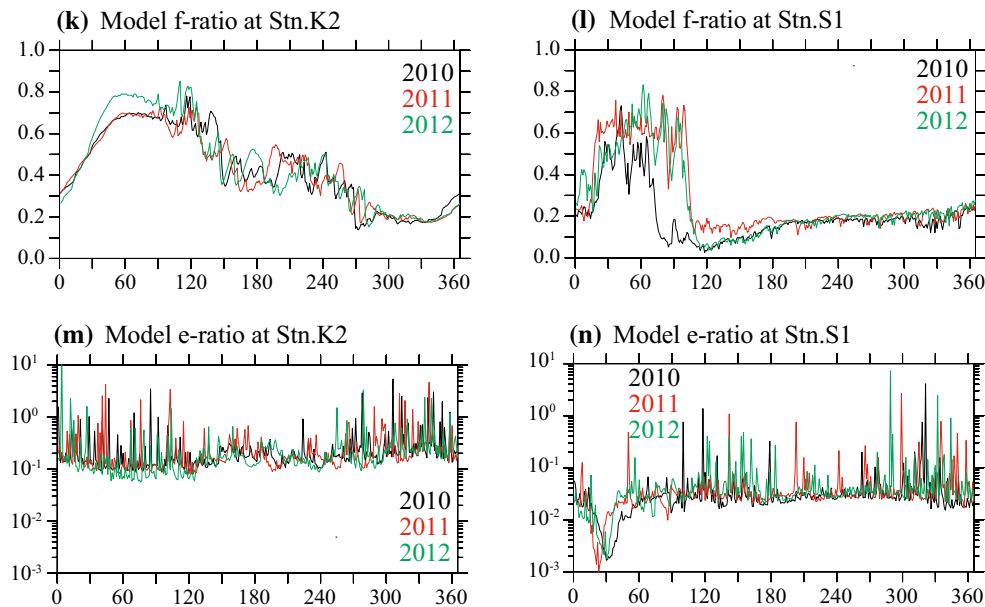


Fig. 8 continued

Table 2 Seasonal and annual averages of depth-integrated primary production ($\text{mg C m}^{-2} \text{ day}^{-1}$) from in situ observation and model at Stn. K2

Stn. K2	In situ obs.	Model, 2010	Model, 2011	Model, 2012	Model, 3 years
Winter (JFM)	109	167	169	141	159
Spring (AMJ)	440	676	586	744	669
Summer (JAS)	556	742	755	608	702
Autumn (OND)	236	252	199	336	262
Annual	335	459	427	457	448

In situ observed primary production averaged from 2005 to 2013 for each season (Matsumoto et al. this volume). Averaged number of model is the same as observed date for each season. Depth-integration of observed primary production is from surface to 0.1 % light depth. Modelled primary production is depth-integrated, 0–150 m

Table 3 Seasonal and annual averages of depth-integrated primary production ($\text{mg C m}^{-2} \text{ day}^{-1}$) from in situ observation and model at Stn. S1

Stn. S1	In situ obs.	Model, 2010	Model, 2011	Model, 2012	Model, 3 years
Winter (JFM)	562	584	643	798	675
Spring (AMJ)	269	58	426	315	266
Summer (JAS)	248	99	194	172	155
Autumn (OND)	108	15	40	37	31
Annual	297	189	326	331	282

In situ observed primary production averaged from 2010 to 2013 for each season (Matsumoto et al. this volume). Averaged number of model is the same as observed date for each season. Depth-integrated of observed primary production is from surface to 0.1 % light depth. Modelled primary production is depth-integrated, 0–200 m.

and the greater nutrient supply results in greater simulated primary production (from 1200 to 2000 $\text{mg C m}^{-2} \text{ day}^{-1}$) (Fig. 8j) and an increase in *f*-ratio from 0.2 to 0.6 (Fig. 8l). In winter, the nutrient supply by the deepening of MLD is an important factor for the surface primary production. After May, the depth-integrated primary production settles between 200 and 400 $\text{mg C m}^{-2} \text{ day}^{-1}$. In the surface layer, chlorophyll disappears after the spring bloom. Then, the subsurface maximum chlorophyll layer forms around the nutricline depth (1.2 $\mu\text{M NO}_3$ line is around 50 m) and primary production remains low. The efficiency of biological pump at Stn. S1 is lower than at Stn. K2 (Fig. 8m, n).

The comparison of seasonally averaged depth-integrated primary production between in situ observations and the model is listed in Table 3 (Stn. S1). The observed primary production is maximal in winter and minimal in autumn, and the modelled primary production agrees with the seasonal variation of observed primary production. From late winter to early spring, the supply of nutrients by the deepening of the MLD is an important factor for sustaining primary production (Fig. 8f, j, l). In 2012, the largest modelled primary production occurs because this year had the deepest MLD of all three years that were simulated. From summer to autumn, the model underestimates primary production by 20–80 % compared to the in situ observations. After the MLD becomes shallow (Fig. 8h, j), the supply of nutrients from the subsurface layer by vertical mixing decreases. One reason for the model's underestimation of summertime production may be that this 1-D physical model only reproduces vertical mixing, while the observed high primary production in summer and autumn may in fact be supported by nutrient supply from 3-D physical processes (horizontal advection and associated upwelling). In the subtropical gyre of the western North Pacific, previous studies have reported that nutrient supply via vertical advection and upwelling associated with mesoscale eddies plays an important role for sustaining primary production in low nutrient seasons (summer and autumn) (e.g., Sasai 2010; Kouketsu 2015).

Modelled primary production at Stn. K2 is greater than that at Stn. S1, and is also greater than the mean of the

observations, which is similar for the two stations. This is because of (1) our assumption of a constant degree of iron limitation throughout the seasonal cycle that results in relatively high values of modelled primary production in summer and fall at Stn. K2, and (2) the sparse coverage of the observations, which do not fully resolve the seasonal cycle, and therefore provide only a rough estimate of the annual average. Further observations are needed to clarify the seasonality of primary production, and to determine precisely how our parameterization of iron limitation in the model may need to be revised.

4 Conclusions

As part of the comparative study, K2S1 project, we have applied a one-dimensional physical–biological model to investigate the mechanisms of seasonal variability of phytoplankton productivity at two contrasting time-series stations in the western North Pacific. The model represents the contrasting seasonal and inter-annual patterns of primary production for these two time-series observation stations, based on the prescribed physical forcing, even though it does not explicitly represent iron limitation, which is known to be important at Stn. K2. This is possible because (1) upwelling of nutrients from below will supply iron as well as macro-nutrients such as nitrate and silicic acid, and (2) we have implicitly parameterized some degree of iron limitation by lowering the maximum growth rate for the model applied to Stn. K2 (Table 1). However, our implicit assumption of a constant degree of iron limitation throughout the year also resulted in an unrealistic autumn bloom at Stn. K2 in the model. Thus, this study has revealed the limits of our approach of assuming a constant degree of iron limitation. More accurate and detailed reproduction of the seasonality of production at locations such as Stn. K2, where there is a seasonal pattern of iron limitation (Fujii 2014), will require explicit modeling of the concentration of bioavailable iron and the iron cycle, with its large associated uncertainties (Boyd and Ellwood 2010; Boyd 2010). Our model does not account for nitrogen fixation, which

may also impact the dynamics at stn. S1, because there is evidence that it occurs in this region. Future studies should also consider the effects of nitrogen fixation in subtropical North Pacific.

The model reproduces two observed characteristics at Stns. K2 and S1: (1) the seasonal variability of primary production at both stations, and (2) the difference in the strength of the biological pump between the two stations. Even though annual primary production at Stn. K2 is comparable to that at Stn. S1, the modelled biological pump at Stn. K2 was more efficient (higher e -ratio in autumn and winter) than at Stn. S1 (Fig. 8k–n).

In our model, the difference in primary productivity between Stns. K2 and S1 results primarily from differences in the physical environment at these two contrasting locations, coupled with the iron limitation at Stn. K2. At Stn. K2 in the subarctic gyre, the light intensity is an important factor limiting primary production in summer. In contrast, at Stn. S1 in the subtropical gyre, the supply of nutrients via entrainment is vital to sustaining production in winter. In summer, the relationship between nutricline depth and euphotic layer is a controlling factor. In addition, the simulations forced by the different atmospheric conditions for each year show different MLD. Deep winter MLD enhances primary production later in the year in the surface layer. Our results show how variations in environmental forcing on the interannual scale, through mechanistic connections, drive interannual differences in primary production at these two contrasting time-series sites.

Acknowledgments This work was partially supported by a CREST project (PI SLS) funded by the Japan Science and Technology Agency. We are also grateful to anonymous reviewers for their constructive and valuable comments.

Appendix: Ecosystem model

The simple nitrogen- and silicon-based plankton ecosystem model, consisting of nine compartments, is coupled with a 1-D physical model of the oceanic mixed layer. The compartments (biological tracers) are nitrate (NO_3), ammonium (NH_4), silicate (Si), two categories of phytoplankton (small phytoplankton, PS and large phytoplankton, PL), zooplankton (Z), dissolved organic nitrogen (DON), particulate organic nitrogen (PON), and bio-silicate (BSi is opal). The evolution of each biological tracer concentration is determined by vertical diffusive mixing using the diffusivity as calculated by the mixed layer model (Mellor and Yamada 1982), and biogeochemical source-minus-sink (sms) terms. The sms terms resulting from biological activity are shown in Fig. 3. Their equations for each individual biological tracer (NO_3 , NH_4 , Si, PS, PL, Z, DON, PON, and BSi) are:

$$\begin{aligned} \text{sms (PS)} &= \text{GppPS}^{(1)} - r_{\text{PS}} \exp(\kappa_{\text{ResPS}} T) \text{PS}^{(3)} \\ &\quad - \mu_{\text{PS}} \exp(\kappa_{\text{MorPS}} T) \text{PS}^{(5)} - \gamma_{\text{PS}} \text{GppPS}^{(7)} - G(\text{PS})Z^{(9)} \end{aligned} \quad (1)$$

$$\begin{aligned} \text{sms (PL)} &= \text{GppPL}^{(2)} - r_{\text{PL}} \exp(\kappa_{\text{ResPL}} T) \text{PL}^{(4)} \\ &\quad - \mu_{\text{PL}} \exp(\kappa_{\text{MorPL}} T) \text{PL}^{(6)} - \gamma_{\text{PL}} \text{GppPL}^{(8)} \\ &\quad - G(\text{PL})Z^{(10)} \end{aligned} \quad (2)$$

$$\begin{aligned} \text{sms (Z)} &= \left(G(\text{PS})Z^{(9)} + G(\text{PL})Z^{(10)} \right) \\ &\quad - (\alpha - \beta)(G(\text{PS})Z + G(\text{PL})Z)^{(11)} \\ &\quad - (1 - \alpha)(G(\text{PS})Z + G(\text{PL})Z)^{(12)} \\ &\quad - \mu_{\text{Z}} \exp(\kappa_{\text{MorZ}} T) Z^{(13)} \end{aligned} \quad (3)$$

$$\begin{aligned} \text{sms (PON)} &= \mu_{\text{PS}} \exp(\kappa_{\text{MorPS}} T) \text{PS}^{(5)} \\ &\quad + \mu_{\text{PL}} \exp(\kappa_{\text{MorPL}} T) \text{PL}^{(6)} \\ &\quad + \mu_{\text{Z}} \exp(\kappa_{\text{MorZ}} T) Z^{(13)} + (1 - \alpha)(G(\text{PS})Z \\ &\quad + G(\text{PL})Z)^{(12)} - \text{VP2N}_0 \exp(\kappa_{\text{P2N}} T) \text{PON} \\ &\quad \times \max(0, \text{PON-R}_{\text{pocsi}} \times (67.2/12) \times R_{\text{nc}} \times \text{Si})^{(14)} \\ &\quad - \text{VP2D}_0 \exp(\kappa_{\text{P2D}} T) \text{PON} \\ &\quad \times \max(0, \text{PON-R}_{\text{pocsi}} \times (67.2/12) \times R_{\text{nc}} \times \text{Si})^{(15)} \\ &\quad - \frac{\partial}{\partial z} (W_s \times \text{PON})^{(18)} \end{aligned} \quad (4)$$

$$\begin{aligned} \text{sms (DON)} &= \gamma_{\text{PS}} \text{GppPS}^{(7)} + \gamma_{\text{PL}} \text{GppPL}^{(8)} \\ &\quad + \text{VP2D}_0 \exp(\kappa_{\text{P2D}} T) \text{PON} \\ &\quad \times \max(0, \text{PON-R}_{\text{pocsi}} \times (67.2/12) \times R_{\text{nc}} \times \text{Si})^{(15)} \\ &\quad - \text{VD2N}_0 \exp(\kappa_{\text{D2N}} T) \text{DON}^{(16)} \end{aligned} \quad (5)$$

$$\begin{aligned} \text{sms (NO}_3) &= - \left(\text{GppPS}^{(1)} - r_{\text{PS}} \exp(\kappa_{\text{ResPS}} T) \text{PS}^{(3)} \right) \text{RnewPS} \\ &\quad - \left(\text{GppPL}^{(2)} - r_{\text{PL}} \exp(\kappa_{\text{ResPL}} T) \text{PL}^{(4)} \right) \text{RnewPL} \\ &\quad + \text{Nit}_0 \exp(\kappa_{\text{Nit}} T) \text{NH}_4^{(17)} \end{aligned} \quad (6)$$

$$\begin{aligned} \text{sms (NH}_4) &= - \left(\text{GppPS}^{(1)} - r_{\text{PS}} \exp(\kappa_{\text{ResPS}} T) \text{PS}^{(3)} \right) (1 - \text{RnewPS}) \\ &\quad - \left(\text{GppPL}^{(2)} - r_{\text{PL}} \exp(\kappa_{\text{ResPL}} T) \text{PL}^{(4)} \right) (1 - \text{RnewPL}) \\ &\quad - \text{Nit}_0 \exp(\kappa_{\text{Nit}} T) \text{NH}_4^{(17)} \\ &\quad + \text{VP2N}_0 \exp(\kappa_{\text{P2N}} T) \text{PON} \\ &\quad \times \max(0, \text{PON-R}_{\text{pocsi}} \times (67.2/12) \times R_{\text{nc}} \times \text{Si})^{(14)} \\ &\quad + \text{VD2N}_0 \exp(\kappa_{\text{D2N}} T) \text{DON}^{(16)} \\ &\quad + (\alpha - \beta)(G(\text{PS})Z + G(\text{PL})Z)^{(11)} \end{aligned} \quad (7)$$

$$\begin{aligned} \text{sms (Si)} &= - \left(\text{GppPL} \times \text{Rsin}^{(19)} - r_{\text{PL}} \exp(\kappa_{\text{ResPL}} T) \text{PL} \times \text{Rsin}^{(20)} \right) \\ &\quad + \gamma_{\text{PL}} \text{GppPL} \times \text{Rsin}^{(21)} \\ &\quad + \text{VP2Si}_0 \exp(\kappa_{\text{P2Si}} T) \text{BSi}^{(24)} \end{aligned} \quad (8)$$

$$\begin{aligned} \text{sms (BSi)} &= \mu_{\text{PL}} \exp(\kappa_{\text{MorPL}} T) \text{PL}^2 \times \text{Rsin}^{(22)} \\ &+ (1 - \alpha)(G(\text{PS})Z + G(\text{PL})Z) \times \text{Rsin}^{(23)} \\ &- \text{VP2Si}_0 \exp(\kappa_{\text{P2Si}} T) \text{BSi}^{(24)} \\ &- \frac{\partial}{\partial z} (W_s \times \text{BSi})^{(25)} \end{aligned} \quad (9)$$

where superscript number (1–25) of biological tracer flux term in each equation is corresponding to biological tracer flux number of Fig. 3. GppPS and GppPL are the absolute values of growth rate (gross primary production), as a function of phytoplankton concentration, depth z , time t , nutrient concentration, N and light intensity. Growth rate depends exponentially on temperature, T , via the so-called Q10 relation, and the light limitation follows Steel (1962). Growth rate depends on nutrient concentrations via Optimal Uptake (OU) kinetics (Pahlow 2005; Smith 2009) as applied, assuming fixed composition of phytoplankton (Shigemitsu 2012). By accounting for physiological acclimation to different nutrient concentrations, OU kinetics has been shown to give a different response under changing environmental conditions, compared to the more widely applied Michaelis-Menten/Monod (MM) equation (Smith 2009; Smith et al. 2010). This results in a saturating dependence of growth rate on nutrient concentration, as for the MM equation, but with a slightly different shape expressed by the following equations:

$$I = I_0 \times \exp(-kz) \quad (12)$$

$$\begin{aligned} k &= 0.04 + 0.054 \times \text{Rnchla} \times (\text{PS} + \text{PL})^{0.667} \\ &+ 0.0088 \times \text{Rnchla} \times (\text{PS} + \text{PL}) \end{aligned} \quad (13)$$

where I_0 is light intensity at the sea surface, and T is water temperature. Small and large phytoplankton (PS and PL in Eqs. 1, 2) are produced by their own growth, and reduced by respiration, mortality, extracellular excretion, and grazing by zooplankton. Grazing rate of phytoplankton by zooplankton is as follows:

$$\begin{aligned} G(\text{PS})Z &= \text{Max}(0, \text{GR}_{\text{max}} \times \exp(\kappa_{\text{GraPS}} T) \\ &\times (1 - \exp(\lambda_{\text{PS}} \times (\text{P2Z} - \text{PS}))) \times Z \end{aligned} \quad (14)$$

$$\begin{aligned} G(\text{PL})Z &= \text{Max}(0, \text{GR}_{\text{max}} \times \exp(\kappa_{\text{GraPL}} T) \\ &\times (1 - \exp(\lambda_{\text{PL}} \times (\text{P2Z} - \text{PL}))) \times Z \end{aligned} \quad (15)$$

Zooplankton (Z in Eq. 3) depends on the grazing rate of Z , excretion rate of Z , egestion rate of Z , and mortality rate of Z . Particulate organic nitrogen (PON in Eq. 4) is produced by mortality (of PS, PL, and Z), and egestion by Z , and is consumed by its decomposition (to NH_4 and DON), and by sinking. Dissolved organic nitrogen (DON in Eq. 5) is produced by extracellular excretion (PS, PL) and decomposition (PON to DON), and is consumed by its remineralization (to NH_4). Nitrate (NO_3 in Eq. 6) is consumed

$$\begin{aligned} \text{GppPS} &= \text{VmaxS} \times \left(\frac{\text{NO}_3}{\text{NO}_3 + \frac{\text{VmaxS}}{A_{\text{NO3PS}}} + 2\sqrt{\frac{\text{VmaxS} \times \text{NO}_3}{A_{\text{NO3PS}}}}} \times \exp(-\varphi_{\text{PS}} \text{NH}_4) + \frac{\text{NH}_4}{\text{NH}_4 + \frac{\text{VmaxS}}{A_{\text{NH4PS}}} + 2\sqrt{\frac{\text{VmaxS} \times \text{NH}_4}{A_{\text{NH4PS}}}}} \right) \\ &\times \exp(\kappa_{\text{GppPS}} T) \\ &\times \int_{-H}^0 \frac{I}{I_{\text{opt}}} \times \exp\left(1 - \frac{I}{I_{\text{opt}}}\right) dz \times \text{PS} \end{aligned} \quad (10)$$

$$\begin{aligned} \text{GppPL} &= \text{VmaxL} \times \text{Min} \left(\frac{\text{NO}_3}{\text{NO}_3 + \frac{\text{VmaxL}}{A_{\text{NO3PL}}} + 2\sqrt{\frac{\text{VmaxL} \times \text{NO}_3}{A_{\text{NO3PL}}}}} \times \exp(-\varphi_{\text{PL}} \text{NH}_4) \right. \\ &+ \left. \frac{\text{NH}_4}{\text{NH}_4 + \frac{\text{VmaxL}}{A_{\text{NH4PL}}} + 2\sqrt{\frac{\text{VmaxL} \times \text{NH}_4}{A_{\text{NH4PL}}}}, \frac{\text{Si}}{\text{Si} + \frac{\text{VmaxL}}{A_{\text{SiPL}}} + 2\sqrt{\frac{\text{VmaxL} \times \text{Si}}{A_{\text{SiPL}}}}} \right) \\ &\times \exp(\kappa_{\text{GppPL}} T) \\ &\times \int_{-H}^0 \frac{I}{I_{\text{opt}}} \times \exp\left(1 - \frac{I}{I_{\text{opt}}}\right) dz \times \text{PL} \end{aligned} \quad (11)$$

by the growth rate of phytoplankton (PS, PL), minus their respiration rate, and produced by nitrification (proportional to NH_4). The f -ratio of phytoplankton (PS, PL) (no dimension) is defined by the ratio of NO_3 uptake to total N ($\text{NO}_3 + \text{NH}_4$) uptake.

$$R_{\text{newPS}} = \frac{\frac{\text{NO}_3}{\text{NO}_3 + \frac{V_{\text{maxS}}}{A_{\text{NO3PS}}} + 2\sqrt{\frac{V_{\text{maxS}} \times \text{NO}_3}{A_{\text{NO3PS}}}} \times \exp(-\varphi_{\text{PS}} \text{NH}_4)}{\frac{\text{NO}_3}{\text{NO}_3 + \frac{V_{\text{maxS}}}{A_{\text{NO3PS}}} + 2\sqrt{\frac{V_{\text{maxS}} \times \text{NO}_3}{A_{\text{NO3PS}}}} \times \exp(-\varphi_{\text{PS}} \text{NH}_4)} + \frac{\text{NH}_4}{\text{NH}_4 + \frac{V_{\text{maxS}}}{A_{\text{NH4PS}}} + 2\sqrt{\frac{V_{\text{maxS}} \times \text{NH}_4}{A_{\text{NH4PS}}}}} \quad (16)$$

$$R_{\text{newPL}} = \frac{\frac{\text{NO}_3}{\text{NO}_3 + \frac{V_{\text{maxL}}}{A_{\text{NO3PL}}} + 2\sqrt{\frac{V_{\text{maxL}} \times \text{NO}_3}{A_{\text{NO3PL}}}} \times \exp(-\varphi_{\text{PL}} \text{NH}_4)}{\frac{\text{NO}_3}{\text{NO}_3 + \frac{V_{\text{maxL}}}{A_{\text{NO3PL}}} + 2\sqrt{\frac{V_{\text{maxL}} \times \text{NO}_3}{A_{\text{NO3PL}}}} \times \exp(-\varphi_{\text{PL}} \text{NH}_4)} + \frac{\text{NH}_4}{\text{NH}_4 + \frac{V_{\text{maxL}}}{A_{\text{NH4PL}}} + 2\sqrt{\frac{V_{\text{maxL}} \times \text{NH}_4}{A_{\text{NH4PL}}}}} \quad (17)$$

The source-sink terms for ammonium (NH_4 in Eq. 7) include the growth rate of phytoplankton (PS, PL), respiration rate (PS, PL), nitrification rate, decomposition rate (PON to NH_4 , DON to NH_4), and excretion rate (Z). Silicate Eq. (8) consumed by the growth of PL (diatoms) minus their respiration and excretion, and is consumed by its dissolution (to Si). Opal (BSi in Eq. 9) is produced by mortality of PL, egestion by Z, and is consumed by its decomposition to Si, and by sinking.

References

- Antonov JI et al (2010) World Ocean Atlas 2009, vol 2: salinity. S. Levitus, Ed. NOAA Atlas NESDIS 69. US Government Printing Office, Washington, DC, pp 184
- Behrenfeld MJ, Falkowski PG (1997) Photosynthetic rates derived from satellite-based chlorophyll concentration. *Limnol Oceanogr* 42:1–20
- Boyd PW et al (2010) Remineralization of upper ocean particles: implications for iron biogeochemistry. *Limnol Oceanogr* 55(3):1271–1288. doi:10.4319/lo.2010.55.3.1271
- Boyd PW, Ellwood MJ (2010) The biogeochemical cycle of iron in the ocean. *Nat Geosci*. doi:10.1038/NGO964
- Buesseler KO et al (2007) Revisiting carbon flux through the oceans twilight zone. *Science* 316:567–570
- Denman KL et al (2006) Modelling the ecosystem response to iron fertilization in the subarctic NE Pacific: the influence of grazing, and Si and N cycling on CO_2 drawdown. *Deep Sea Res II* 53:2327–2352
- Denman KL, Peña MA (1999) A coupled 1-D biological/ physical model of the Northeast Subarctic Pacific Ocean with iron limitation. *Deep Sea Res II* 46:2877–2908
- Fujii M et al (2002) A one-dimensional ecosystem model applied to time-series Station KNOT. *Deep Sea Res II* 49:5441–5461
- Fujiki T et al (2014) Seasonal cycle of phytoplankton community structure and photophysiological state in the western subarctic gyre of the North Pacific. *Limnol Oceanogr* 59(3):887–900. doi:10.4319/lo.2014.59.3.0887
- Garcia HE et al. (2010) World Ocean Atlas 2009, vol 4: nutrients (phosphate, nitrate, silicate). S. Levitus, Ed. NOAA Atlas NESDIS 71. US Government Printing Office, Washington, DC, pp 398
- Goes JI et al (2004) A comparison of the seasonality and interannual variability of phytoplankton biomass and production in the western and eastern gyres of subarctic Pacific using multi-sensor satellite data. *J Oceanogr* 60:75–91
- Harrison PJ et al (2004) Nutrient and plankton dynamics in the NE and NW gyres of the subarctic Pacific Ocean. *J Oceanogr* 60:93–117. doi:10.1023/B:JOCE.0000038321.57391.2a
- Honda MC et al (2016a) Overview of Study of change in ecosystem and material cycles by the climate change based on time-series observation in the western North Pacific: K2S1 project (this volume, a)
- Honda MC et al (2016b) A comparison of fluxes and characteristics of sinking particles in mesopelagic / bathypelagic layer between subarctic station K2 and subtropical station S1 based on moored time-series sediment trap experiment (this volume)
- Honda MC et al (2002) The biological pump in the northwestern North Pacific based on fluxes and major components of particulate matter obtained by sediment trap experiments (1997–2000). *Deep Sea Res II* 49:5595–5625
- Honda MC et al (2006) Quick transport of primary production organic carbon to the ocean interior. *Geophys Res Lett* 33:L16603. doi:10.1029/2006GL026466
- Honda MC et al (2015) Comparison of sinking particles in the upper 200 m between subarctic station K2 and subtropical station S1 based on drifting sediment trap experiments. *J Oceanogr*. doi:10.1007/s10872-015-0280-x
- Honda MC, Watanabe S (2010) Importance of biogenic opal as ballast of particulate organic carbon (POC) transport and existence of mineral ballast-associated and residual POC in the Western Pacific Subarctic Gyre. *Geophys Res Lett* 37:L02605. doi:10.1029/2009GL041521
- Kawakami H et al (2014) Time-series observations of ^{210}Po and ^{210}Pb radioactivity in the western North Pacific. *J Radioanal Nucl Chem* 301:461–468. doi:10.1007/s10967-014-3141-y
- Kawakami H, Honda MC (2007) Time-series observation of POC fluxes estimated from ^{234}Th in the northwestern North Pacific. *Deep Sea Res I* 54(7):1070–1090
- Kawamiya M et al (1997) Procuring reasonable results in different oceanic regimes with the same ecological–physical coupled model. *J Oceanogr* 53:397–402
- Kishi MJ et al (2007) NEMURO: a lower trophic level model for the North Pacific marine ecosystem. *Ecol Model* 202:12–25
- Kouketsu S et al (2015) Mesoscale eddy effects on temporal variability of surface chlorophyll a in the Kuroshio Extension. *J Oceanogr*. doi:10.1007/s10872-015-0286-4
- Locarnini RA et al (2010) World Ocean Atlas 2009, vol 1: temperature. S. Levitus, Ed. NOAA Atlas NESDIS 68. US Government Printing Office, Washington, DC, pp 184

- Martin J et al (1994) Testing the iron hypothesis in ecosystem of the equatorial Pacific Ocean. *Nature* 5:1–13
- Matsumoto K et al (2016) Primary productivity at the time-series stations in the northwestern Pacific Ocean: Is the subtropical station unproductive? (this volume)
- Matsumoto K et al (2014) Seasonal variability of primary production and phytoplankton biomass in the western Pacific subarctic gyre. Control by light availability within the mixed layer. *J Geophys Res Ocean* 119:6523–6534. doi:[10.1002/2014JC009982](https://doi.org/10.1002/2014JC009982)
- Mellor GL, Yamada T (1982) Development of a turbulence closure model for geophysical fluid problems. *Rev Geophys Space Phys* 20:851–875
- Moore JK, Doney SC, Lindsay K (2004) Upper ocean ecosystem dynamics and iron cycling in a global three-dimensional model. *Glob Biogeochem Cycles* 18:GB4028. doi:[10.1029/2004GB00220](https://doi.org/10.1029/2004GB00220)
- Onogi K et al (2007) The JRA-25 reanalysis. *J Meteorol Soc Jpn* 85:369–432. doi:[10.2151/jmsj.85.369](https://doi.org/10.2151/jmsj.85.369)
- Pahlow M (2005) Linking chlorophyll–nutrient dynamics to the Redfield N:C ratio with a model of optimal phytoplankton growth. *Ecol Prog Ser* 287:33–43. doi:[10.3354/meps287033](https://doi.org/10.3354/meps287033)
- Parekh P, Follows MJ, Boyle E (2002) Modeling the global ocean iron cycle. *Glob Biogeochem Cycles* 18:GB1002. doi:[10.1029/2003GB002061](https://doi.org/10.1029/2003GB002061)
- Sarmiento JL et al (1993) A seasonal three-dimensional ecosystem model of nitrogen cycling in the North Atlantic euphotic zone. *Glob Biogeochem Cycles* 7:417–450
- Sasai Y et al (2010) Effects of cyclonic eddies on the marine ecosystem in the Kuroshio Extension region using an eddy-resolving coupled physical–biological model. *Ocean Dyn* 60(3):693–704. doi:[10.1007/s10236-010-0264-8](https://doi.org/10.1007/s10236-010-0264-8)
- Sasaoka K et al (2002) Temporal and spatial variability of chlorophyll-a in the western subarctic Pacific determined from satellite and ship observations from 1997 to 1999. *Deep Sea Res II* 49:5557–5576
- Shigemitsu M et al (2012) Development of a one-dimensional ecosystem model including the iron cycle applied to the Oyashio region, western subarctic Pacific. *J Geophys Res* 117:C06021. doi:[10.1029/2011JC007689](https://doi.org/10.1029/2011JC007689)
- Siswanto E et al (2014) Reappraisal of meridional differences of factors controlling phytoplankton biomass and initial increase preceding seasonal bloom in the northwestern Pacific Ocean. *Remote Sens Environ* 159:44–56. doi:[10.1016/j.rse.2014.11.028](https://doi.org/10.1016/j.rse.2014.11.028)
- Smith SL et al (2009) Optimal uptake kinetics: physiological acclimation explains the observed pattern of nitrate uptake by phytoplankton in the ocean. *Mar Ecol Prog Ser* 384:1–12. doi:[10.3354/meps08022](https://doi.org/10.3354/meps08022)
- Smith SL, Yoshie N, Yamanaka Y (2010) Physiological acclimation by phytoplankton explains observed changes in Si and N uptake rates during the SERIES iron-enrichment experiment. *Deep Sea Res I* 57:394–408. doi:[10.1016/j.dsr.2009.09.009](https://doi.org/10.1016/j.dsr.2009.09.009)
- Steel JH (1962) Environmental control to phytoplankton in sea. *Limnol Oceanogr* 7:137–172
- Takeda S et al (2006) Modeling studies investigating the causes of preferential depletion of silicic acid relative to nitrate during SERIES: a mesoscale iron-enrichment in the NE subarctic Pacific. *Deep Sea Res II* 53:2297–2326
- Tsuda A et al (2003) A mesoscale iron enrichment in the western subarctic Pacific induces large centric diatom bloom. *Science* 300:958–961. doi:[10.1126/science.1082000](https://doi.org/10.1126/science.1082000)
- Wakita M et al (2016) Biological organic carbon export estimated from annual carbon budget in the surface water of western subarctic and subtropical North Pacific Ocean (this volume)
- Yoshikawa C, Yamanaka Y, Nakatsuka T (2005) An ecosystem model including nitrogen isotopes: perspectives on a study of the marine nitrogen cycle. *J Oceanogr* 61:921–942